Combustion and Flame 214 (2020) 464–474

Contents lists available at ScienceDirect

Combustion and Flame

journal homepage: www.elsevier.com/locate/combustflame

Laminar flame speed, Markstein length, and cellular instability for spherically propagating methane/ethylene–air premixed flames

Hee J. Kim[a], Kyuho Van[a], Dae K. Lee[b], Chun S. Yoo[c,*], Jeong Park[a,*], Suk H. Chung[d]

[a] Department of Mechanical Engineering, Pukyong National University, Busan, Korea
[b] Advanced Combustion Lab, Korea Institute of Energy Research, Daejeon, Korea
[c] Department of Mechanical Engineering, Ulsan National Institute of Science and Technology (UNIST), Ulsan, Korea
[d] Clean Combustion Research Center (CCRC), King Abdullah University of Science and Technology (KAUST), Thuwal, Saudi Arabia

ARTICLE INFO

Article history:
Received 2 August 2019
Revised 23 September 2019
Accepted 10 January 2020

Keywords:
Cellular instability
Critical flame radius
Laminar flame speed
Markstein length
Methane/ethylene

ABSTRACT

An experimental study on laminar flame speed, Markstein length, and the onset of cellular instability was conducted by varying the equivalence ratio and ethylene/methane mixing ratio in spherically propagating premixed flames at ambient temperature and elevated pressures up to 0.8 MPa. Unstretched laminar burning velocities were first validated for methane – air flames by optimizing the range of the flame radius in testing linear and non-linear extrapolation models, and subsequently comparing the results with those simulated using four kinetic mechanisms. Based on the results, unstretched laminar burning velocities were determined for premixed flames of methane/ethylene mixture fuels. The predictability of theoretical Markstein lengths was appreciated by adopting a composite solution of the heat-release-weighted Lewis number and the temperature-dependent Zel'dovich number. Measured Markstein lengths were compared with those predicted based on a composite model for laminar flame speeds against flame radius. Depending on the fuels (methane or methane/ethylene mixture), pressure, and equivalence ratio, the predictability of the model varied. For methane – air flames, cellular instabilities were not observed within the observation window at pressures up to 0.6 MPa. Cell formation, caused by hydrodynamic instability, was enhanced by an increase in the ethylene ratio and chamber pressure. Theoretical critical flame radii for the onset of cellular instability predicted by the composite model were consistent with the measured ones for both lean and rich mixtures.

1. Introduction

Natural gas, with methane as a major constituent, supplies 22% of the energy used worldwide, and contributes nearly a quarter of the electricity generated [1]. The growth in the natural gas supply is linked, in part, to its environmental benefits relative to other hydrocarbon fuels, particularly for air quality as well as climate change. Various industrial burners and gas turbine combustors have been designed and developed to meet many requirements, including high efficiency over a wide range of operating conditions and low NOx and smoke emissions. Particularly, stringent regulations limit NOx emission for stationary sources (e.g., industrial burners, power plants, and boilers) and mobile sources (e.g., engines and gas turbines). Applying lean-burn technology with natural gas to such combustion systems may fulfill low NOx and CO_2 emission requirements. However, lean-burn natural gas systems have been limited by flame stability [2–4]. Several proposals have been put forward to address the stability issue, such as blending hydrogen (or H_2/CO syngas) with methane, resulting in an extension of lean flammable limit, and thereby a reduction of NO emission [5–7].

Ethylene, as one of the major components in practical fuels [8–10], has much better improved burning velocity and ignition temperature characteristics than methane [8–10]. In this regard, ethylene flames have been studied to understand the fundamental combustion characteristics, e.g., ignition temperature and laminar burning velocity [8] and chemical structures [9]. Although ethylene could play a role similar to hydrogen when mixed with methane, in terms of laminar burning velocity and ignition temperature, research on this has been rather limited; some studies have explored laminar burning velocities of the mixture fuels of methane and ethylene [8] and the effects of additional diluents (CO_2 and He) and chamber pressure (up to 0.3 MPa) on unstretched laminar burning velocity and Markstein length in outwardly propagating spherical flames with the blended fuel of 50% CH_4 and 50% C_2H_4 in volume [11].

* Corresponding authors.
E-mail addresses: csyoo@unist.ac.kr (C.S. Yoo), jeongpark@pknu.ac.kr (J. Park).

https://doi.org/10.1016/j.combustflame.2020.01.011
0010-2180/

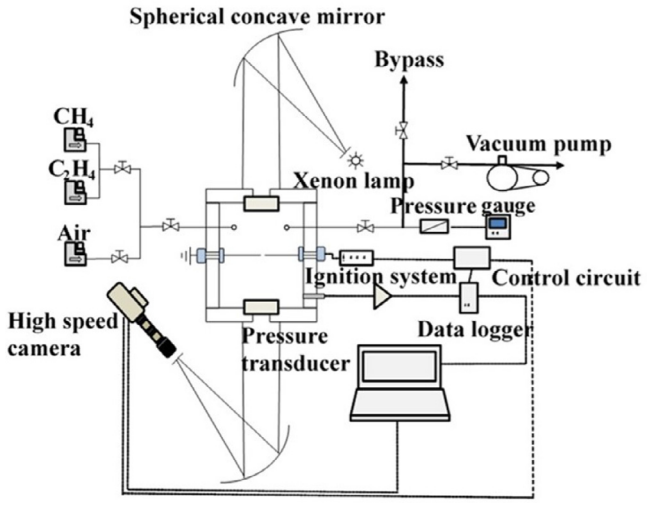

Fig. 1. Schematic diagram of the experimental setup.

The present study focused on three important characteristics of premixed flame: laminar burning velocity, Markstein length, and cellular instability, by varying mixture composition, equivalence ratio, and ambient pressure (up to 0.8 MPa) in outwardly propagating spherical premixed flames for blended fuels of CH_4 and C_2H_4 with an ethylene mixing ratio (in volume) ranging from 0 to 0.3. An experimental determination of unstretched laminar burning velocity S_u^o depends strongly on the choice of extrapolation method from the measured stretched flame speed [12–23]. The present study first examined extrapolation methods for methane–air premixed flames by comparing measured data with existing data [12–23] and conducting numerical simulations with four kinetic mechanisms of GRI v-3.0 [24], USC Mech II [25], Sung Mech [26], and Aramco 2.0 [27]. An optimized method was applied to the present methane/ethylene mixture flames.

Laminar burning velocity is a key parameter in understanding flame characteristics in practical spark-ignition engines and gas turbine combustors. Because practical flames are either curved and/or propagate through a strained flow field, the Markstein length [28–36], which quantifies the response of flame speed to stretch rate, also plays an important role in characterizing flame behavior. Even in the absence of initial turbulence, spherical flames could form a cellular structure due to diffusive-thermal and hydrodynamic instabilities [37–46], resulting in flame acceleration with an increase in flame surface area. In this regard, Markstein length and cellular instability have been studied extensively. These have been investigated for several blended fuels such as methane-hydrogen, and syngas and bio-syngas mixtures as well as diluted fuels [11,47–50]. However, those for the blended fuels of methane and ethylene have not been investigated in detail, and are therefore the focus of the present study. Here, theoretical and measured Markstein lengths are compared and discussed, and cellular instabilities are evaluated by comparing theoretical and measured critical flame radii for cell formation.

2. Experiment

Details of a similar experimental setup and method are described in our previous work. Here, as schematically shown in Fig. 1 [11], a larger stainless steel cylindrical constant-volume combustion chamber (CVCC) was used (inner diameter: 300 mm; length: 390 mm). Two quartz windows (diameter: 150 mm) were installed for visualization. Methane (purity 99.99%) and ethylene (99.99%) were used for the fuel, and zero air (99.95%) was used as the oxidizer. Fuel and air were metered from partial pressures using a pressure gauge (LabDMM AEP, −1 to 40 bar, ± 0.5% FSO). Outwardly propagating spherical flames were visualized using a Schlieren setup with a 300-W xenon light source and a pair of concave mirrors (diameter: 150 mm), taken by a high-speed camera (Phantom v-7.2) at 10,000 frames per second (fps). The position of the flame front was determined by converting to a monochromatic image to accommodate the IMADJUST function in Matlab software for image enhancement [11]. The image was subsequently binarized (with a center intensity of 127 as a threshold from the monochromatic intensity range of $0-255$), from which the flame front position was identified. This arbitrary choice of the threshold value did not affect the determination of the laminar burning velocity. The initial pressure range covered up to $P_0 = 0.8$ MPa.

3. Results and discussion

3.1. Determination of unstretched laminar burning velocity

The time history of the flame front radius, $R_f(t)$, for an outwardly propagating spherical flame can be obtained using the Schlieren method. With the assumption of a static burnt gas inside the spherical flame, the stretched burnt flame speed, S_b, becomes $S_b = dR_f/dt$. When the spherical flame is assumed to be infinitesimally thin, weakly stretched, quasi-steady, and zero-gravity in an unconfined environment, the unstretched laminar burning velocity, S_b^o, with respect to the burnt mixture can be obtained via the following linear extrapolation model (LM) [11–23]:

$$S_b = S_b^o - L_b K \tag{1}$$

where L_b denotes the Markstein length with respect to the burnt gas, which can be determined experimentally from the slope of S_b with flame stretch, $K = 2S_b/R_f$, and S_b^o through the extrapolation to $K = 0$. Then, the unstretched laminar burning velocity, S_u^o, with respect to the unburned mixture can be determined from the mass conservation of $S_u^o = (\rho_b/\rho_u)S_b^o$, where ρ_b and ρ_u are the densities of the burnt and unburned mixtures, respectively.

Because errors with the LM could arise, especially when the equivalence ratio deviates appreciably from unity [12], the following two nonlinear models (NM I and NM II) are proposed:

$$S_b = S_b^o - \frac{2S_b^o L_b}{R_f} \text{ or } S_b = S_b^o - L_b K\left(\frac{S_b^o}{S_b}\right) \text{ (NM I)}, \tag{2}$$

$$ln\ S_b = \ln S_b^o - S_b^o L_b \times \frac{2}{R_f S_b} \text{ (NM II)}. \tag{3}$$

NM I was proposed by Markstein [31] and analyzed by Frankel and Sivashinsky [32] in propagating spherical flames, where S_b varies nonlinearly with K. Note that S_b is linear with the flame curvature $2/R_f$, through which L_b and S_b^o can be determined from a linear extrapolation. NM II has been derived for quasi-steady and adiabatic flame conditions using an asymptotic method [33,34], and its validity in predicting S_b^o has been tested previously [35]. Here, $\ln S_b$ varies linearly with $2/R_f S_b$; thus, L_b and S_b^o can be determined by a linear extrapolation from the plot of $\ln S_b$ against $2/R_f S_b$. Note that the LM and NM I can be derived readily from NM II in the limit of a large flame radius, with accuracies of the order of $O(1/R_f^2)$ representing the error [51,52].

Choice of an appropriate extrapolation model depends on the size of the combustion chamber and the range of flame radius to be used in the extrapolation. When the smaller CCVC (as compared with the present one) was used previously [11], NM II provided the best performance in determining laminar burning velocities from simulated results using GRI v-3.0 for methane–air premixed flame under normal temperature and pressure (NTP) conditions. For further confirmation with the present chamber

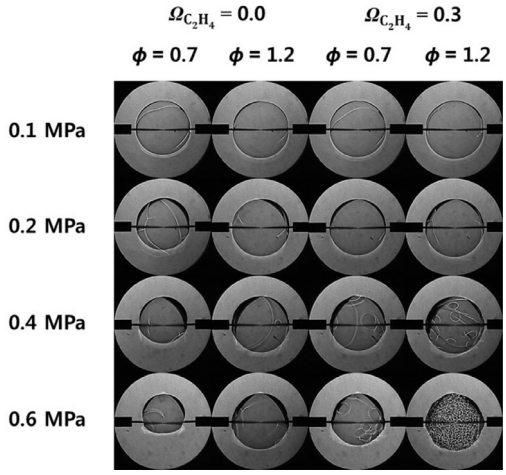

Fig. 2. Instantaneous Schlieren images of CH_4–air ($\Omega_{C_2H_4} = 0$) and CH_4/C_2H_4–air ($\Omega_{C_2H_4} = 0.3$) premixed flames with $\phi = 0.7$ and 1.2 at various initial chamber pressures.

size, we extensively re-evaluated the results for methane–air premixed flames at NTP by comparing measured data with existing data [12–23], along with simulation data with four kinetic mechanisms of GRI v-3.0 [24], USC Mech II [25], Sung Mech [26], and Aramco 2.0 [27]. By excluding the effects of spark-ignition transient, chamber confinement, and cellular instability, the flame radius monitored was taken over the range of $13.0 \leq R_f \leq 31.0$ mm (see the detailed discussion concerning Figs. S1–S5 and Table S1 in the Supplementary Material (SM)). At various equivalence ratios ϕ for $P_0 = 0.1$ and 0.6 MPa, the results revealed that NM II was appropriate in the present study and that Aramco Mech 2.0 best fit the measured laminar burning velocities.

For further confirmation, measured laminar burning velocities with equivalence ratio for CH_4–air premixed flames were compared with numerical simulations with Aramco Mech 2.0 (Fig. S6) at several ambient pressures. The measured data were in good agreement with numerical simulations. Given the validity of the present methodology for methane fuels, fuel mixtures of methane and ethylene were investigated as described in the following.

3.2. Laminar flame speeds for CH_4/C_2H_4–air premixed flames

Instantaneous Schlieren images of CH_4–air (first and second columns for $\Omega_{C_2H_4} = 0$) and CH_4/C_2H_4–air (third and fourth columns for $\Omega_{C_2H_4} = 0.3$) premixed flames are compared in Fig. 2 at $\phi = 0.7$ and 1.2 for several initial chamber pressures. Here, the ethylene mixing ratio ($\Omega_{C_2H_4}$) is defined as $\Omega_{C_2H_4} = X_{C_2H_4}/(X_{CH_4} + X_{C_2H_4})$ where X_i is the mole fraction of species i. The images were obtained when the radius of the uppermost flame edge was about 45 mm from the ignition point. The CH_4–air cases generally had smooth flame surfaces, except for some large-scale cracks (typically observed in spherically propagating flames [41,43–46]) up to $P_0 = 0.6$ MPa for both $\phi = 0.7$ and 1.2. For the CH_4/C_2H_4–air flames, the surfaces were smooth overall, with the exception of $P_0 = 0.6$ MPa and $\phi = 1.2$, in which fine cellular structures were observed. These finding will be discussed in the sections that follow.

Buoyancy effects in measuring unstretched laminar burning velocities are considered to be weak in cases with $S_u^0 > 15$ cm/s [16–27], compared with other error sources [12]. However, as the pressure becomes large, such a flame can be influenced appreciably by buoyancy, because S_u^0 decreases with pressure. This is exemplified by the cases of $\phi = 0.7$ at $P_0 = 0.4$ and 0.6 MPa for

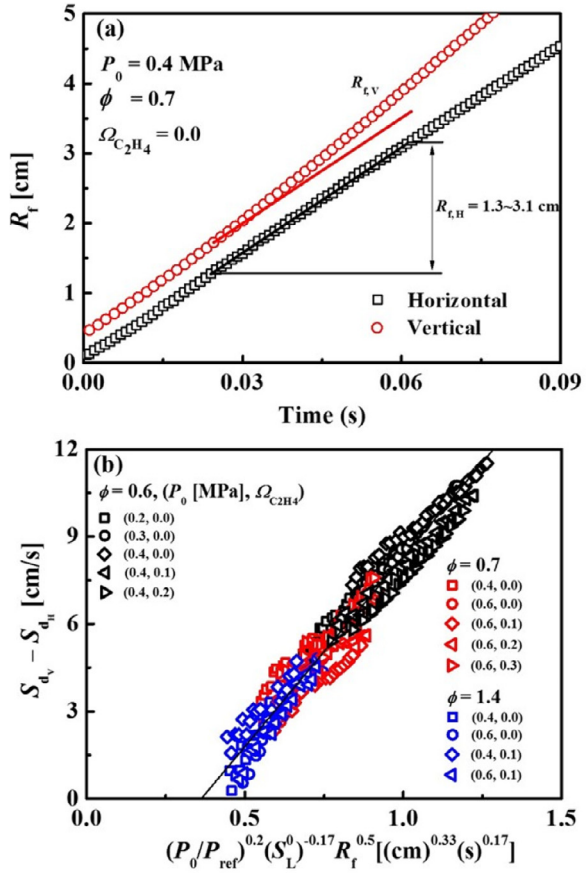

Fig. 3. Influence of buoyancy on flame speed with respect to burnt gas: (a) typical time histories of horizontal and vertical flame radii at $\phi = 0.7$ and $P_0 = 0.4$ MPa for $\Omega_{C_2H_4} = 0$ and (b) parameter dependence of the buoyancy-induced velocity component.

$\Omega_{C_2H_4} = 0$ in Fig. 2. Although sphericity is reasonably maintained, the center of the flame moves upward appreciably.

Figure 3a presents typical time histories of flame radii in the horizontal ($R_{f,H}$) and vertical ($R_{f,V}$) directions for $\phi = 0.7$ and $P_0 = 0.4$ MPa when $\Omega_{C_2H_4} = 0$; compared with the horizontal radius, the vertical flame radius accelerates over time, as marked with solid lines for $R_f = 1.3 - 3.1$ cm. Assuming that buoyancy-induced flow acts mainly in the vertical direction, the horizontal displacement velocity can be approximated as the burnt flame speed. In such a case, the magnitude of buoyancy-induced vertical velocity can be approximated as the difference between the vertical and horizontal burnt displacement speeds ($S_{d,V} - S_{d,H}$).

For future data reduction on laminar burning velocity from outwardly propagating spherical flames, we correlated the buoyancy-induced vertical velocity based on our experimental data for $\phi = 0.6$, 0.7, and 1.4 at various initial pressures and ethylene mixing ratios. The horizontal burnt flame speed was obtained from the rate of change of the flame front with time over the range of $13.0 \leq R_{f,H} \leq 31.0$ mm, excluding the effects of spark-ignition, and thereby ignition transient and chamber confinement effects. The vertical burnt flame speed was also obtained using a similar approach. Buoyancy effects can also be enhanced for a small laminar burning velocity (longer residence time for the buoyancy effect to develop), a large initial chamber pressure, and a large flame radius. The buoyancy-induced velocity component ($S_{d,V} - S_{d,H}$), is correlated with the parameters of P_0, S_L^0, and R_f. The best fit corresponded to $(S_{d,V} - S_{d,H})$ [cm/s] = $13.0 \times (P_0/P_{ref})^{0.17}(S_L^0)^{-0.17} R_f^{0.5} - 4.7$ with a correlation coefficient

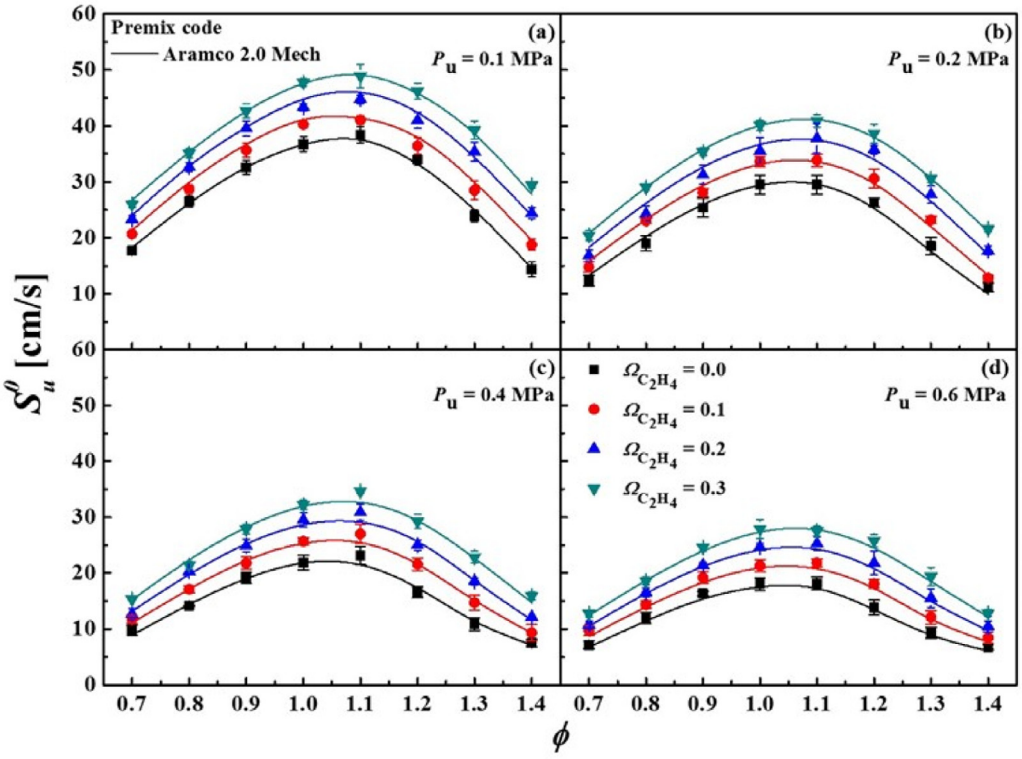

Fig. 4. Experimental and predicted unstretched laminar burning velocities against equivalence ratio in CH_4/C_2H_4–air premixed flames at various $\Omega_{C_2H_4}$ for P_0 = 0.1 (a), 0.2 (b), 0.4 (c), and 0.6 (d) MPa. Solid lines represent simulated data using PREMIX code [49] with Aramco Mech 2.0 [27].

of $R = 0.98$, where P_{ref} is the atmospheric pressure (0.1 MPa) and S_L^0 and R_f are given units of [cm/s] and [cm], respectively. The results presented in Fig. 3b show a satisfactory correlation. More precise buoyancy-induced velocity may be obtained through the local flow velocity at the center, and this will be a future work.

For further confirmation of the three extrapolation models in CH_4/C_2H_4-air premixed flames, the burnt flame speed versus flame stretch was again tested at various equivalence ratios for $\Omega_{C_2H_4}$ = 0.3 (see Fig. S7 at P_0 = 0.1 MPa and Fig. S8 at P_0 = 0.6 MPa in the SM). NM II best traced to measured burnt flame speeds, as shown in Figs. S7 and S8. The results of uncertainty were also summarized in Table S2 for CH_4/C_2H_4–air premixed flames ($\Omega_{C_2H_4}$ = 0.3) with P_0 = 0.1, 0.4, and 0.6 MPa, when the four kinetic mechanisms [24–27] were adopted again. The results showed that using Aramco 2.0 resulted in the smallest errors among them. Again, NM II and Aramco 2.0 were adopted again in CH_4/C_2H_4-air premixed flames.

Figure 4 presents laminar burning velocities as a function of equivalence ratio for the CH_4/C_2H_4–air premixed flames at several initial pressures and ethylene mixing ratios, along with simulation data using PREMIX code [51] by adopting Aramco Mech 2.0. The error bars denote the maximum and minimum values taken from six experiments for each condition. Note that the monitored range of flame radius was $13.0 \le R_f \le 31.0$ mm in the present experiment. As shall be shown later, even at ϕ = 1.2 for P_0 = 0.6 MPa (Fig. 2), the experimental critical radius for the onset of cellular instability is larger than 31 mm (maximum flame radius monitored). Thus, unstretched laminar burning velocity could be measured. The laminar burning velocity increased (decreased) with the increase of $\Omega_{C_2H_4}(P_0)$. The results also revealed that the numerical simulation results at various initial pressures and ethylene mixing ratios for CH_4/C_2H_4–air premixed flames were in good agreement with the present experimental ones, despite the appreciable deviation in the equivalence ratio from unity when determining S_u^0 from the horizontal radius. In the following, Aramco Mech 2.0 will be used in evaluating the theoretical Markstein length and critical flame radius for cellular instability.

3.3. Markstein length in CH_4/C_2H_4–air premixed flames

A Markstein length characterizes the effect of flame stretch on laminar flame speed. Two theoretical models [52,53] for evaluating Markstein length with respect to burnt gas were applied to CO_2- and He-diluted CH_4/C_2H_4–air premixed flames with $\Omega_{C_2H_4}$ = 0.5 [11] up to P_0 = 0.3 MPa. The results revealed that the model of Bechtold and Matalon [53] better predicted the measured Markstein length.

However, these models are applicable for infinitely thin, weakly stretched flames. When considering the finite flame thickness, one must account for the variation of the flow field in the preheat zone such that the corresponding Markstein number along the flame thickness could vary by $O(1)$ despite the small flame thickness. For comparison with experimental and/or numerical simulation data, the composite model valid within and outside the flame zone was derived by an asymptotic method [54]. Since the details of the composite solution can be found in [54], a brief explanation is made here.

At any location within a flame zone in outwardly-propagating spherical flame, the theoretical Markstein length [54] can be obtained as:

$$L^* = \left\{ \alpha - \int_1^{\theta^*} \frac{\lambda(x)}{x} dx - \frac{\sigma - 1}{\sigma} \int_{\theta^*}^{\sigma} \frac{\lambda(x)}{x - 1} dx \right\}, \quad (4)$$

where

$$\alpha = \frac{\sigma}{\sigma - 1} \int_1^{\sigma} \frac{\lambda(x)}{x} dx + \frac{\beta(\mathrm{Le_{eff}} - 1)}{2(\sigma - 1)} \int_1^{\sigma} \ln\left(\frac{\sigma - 1}{x - 1}\right) \frac{\lambda(x)}{x} dx$$

Here $\sigma = \rho_u/\rho_b$ is the thermal expansion ratio, $\beta = E(T_b - T_u)/RT_b^2$ is the Zel'dovich number, $\theta^* = T^*/T_u$ is the dimensionless

temperature at the location of iso-surface taken as the flame front, Le_{eff} is the effective Lewis number of the mixture, and λ is the thermal conductivity of the mixture scaled with respect to its value in the unburned gas, respectively.

The errors for unstretched laminar burning velocity and Markstein length were previously shown to be within 10% and 200%, respectively [52]. This explains the relatively consistent laminar burning velocities measured by various groups (see Figs. S5 and S7, and [52]), whereas large discrepancies in the Markstein lengths were evident, even at normal pressure (see Fig. S6 and [52]). Evaluating theoretical Markstein lengths via a comparison with measured values has generally been conducted at normal pressure [13,14,17,18,20,52,53,54]. Special care must be taken at elevated pressures when using the theoretical model.

The Zel'dovich number β_T, with a temperature-dependent activation energy ($Ea_T = -2R^0\pi[\partial ln(\rho_u S_u^o)/(\partial(1/T_{ad})]$) [43–46] and a heat-release-weighted fuel Lewis number ($Le_{F,q} = 1 + (q_{CH_4}(Le_{CH_4} - 1) + q_{C_2H_4}(Le_{C_2H_4} - 1))/q$) [43–46], was used for the calculation of the theoretical Markstein length, because predictions using these have proven to be more accurate [11]. Here, q is the total heat release ($q = q_{CH_4} + q_{C_2H_4}$), where q_i is the non-dimensional heat release associated with the consumption of species i ($q_i = QY_i/C_pT_u$), Q is the heat of reaction, and Y_i is the mass fraction of species i. When a single-component fuel is used, the two fuel Lewis numbers become the same. Note that both theoretical models are derived based on a deficient reactant concept. Thus, using such fuel Lewis numbers (as an effective Lewis number) may yield a good prediction of Markstein length under lean mixture conditions. Although the capability of predicting Markstein length can be restricted near stoichiometric or rich conditions, such a problem can be mitigated using the effective Lewis number $Le_q = 1 + (Le_E - 1) + A_1(Le_D - 1)/(1 + A_1)$, through $Le_{E,q}$ [38]. Here, Le_E and Le_D are the Lewis numbers of abundant and deficient reactants, respectively. The parameter A_1 is a measure of mixture strength, defined as $A_1 = 1 + \beta(\Phi - 1)$. Φ is the ratio of the masses of abundant-to-deficient reactants in the fresh mixture relative to their stoichiometric ratio, i.e., $\Phi = 1/\phi$ for $\phi \le 1$ and $\Phi = \phi$ for $\phi > 1$. Heat-release-rate- and volume-weighted effective Lewis numbers (Le_q, Le_V), constant and temperature-dependent Zel'dovich numbers (β_{const}, β_T), thermal expansion ratio (σ) used in predicting Markstein lengths in CH_4-air and CH_4/C_2H_4–air premixed flames at various equivalence ratios are presented in Table S3 in the SM.

The theoretical Markstein lengths were first compared with the measured ones for CH_4-air premixed flames at normal and elevated pressures (see Figs. S9-S12 in SM). The results show that the theoretical Markstein lengths are in good agreement with the present measured data when the iso-temperature is 600 K, the non-dimensional thermal conductivity is taken as $\lambda(x) = x$, and the flame thickness is defined by $\delta_f^0 = (T_b - T_u)/(\partial T/\partial x)_{max}$. Based on them, measured and predicted Markstein numbers against equivalence ratio were compared in terms of ambient pressure for CH_4–air premixed flames with $\lambda(x) = x$ for $\delta_f^0 = (\lambda/c_p)/(\rho_u S_u^o)$ and $(T_b - T_u)/(\partial T/\partial x)_{max}$ (see Fig. S13 in the SM). When $\delta_f^0 = (T_b - T_u)/(\partial T/\partial x)_{max}$ is used, the theoretical Markstein numbers better traces the measured data. The measured Markstein number decreases appreciably (slightly) when the ambient pressure varies from 0.1 to 0.2 (0.2 to 0.6) MPa, while the theoretical Markstein numbers are not influenced by ambient pressure. This implies that the theoretical Markstein number does not reflect the effect of reducing flame thickness. Further discussion on the effect of using the different definitions in flame thickness will be made later. The effect of using different effective Lewis numbers on Markstein length was tested in terms of ambient pressures for CH_4-air premixed flame (see Fig. S13 in the SM). The results show that the effects are minor at normal and elevated pressures.

Further investigation on the capability of predicting Markstein length was made in CH_4/C_2H_4-air premixed flames, by again varying the iso-temperature of flame front and using the different definition of flame thickness for $\lambda(x) = x$. Although not shown, we tested the effect of non-dimensional thermal conductivity defined differently with $\lambda(x) = 1$, $x^{1/2}$, and x. When $\lambda(x) = x$ is used, the theoretical Markstein lengths better trace the measured ones. Thus, the effect of using the definitions of different flame thickness and elevated ambient pressures on Markstein length is investigated for CH_4/C_2H_4-air premixed flames with $\delta_f^0 = (\lambda/c_p)/(\rho_u S_u^o)$ in Fig. 5 and with $\delta_f^0 = (T_b - T_u)/(\partial T/\partial x)_{max}$ in Fig. 6. The theoretical Markstein lengths with $\delta_f^0 = (T_b - T_u)/(\partial T/\partial x)_{max}$ are in better agreement with the measured data, compared with those with $\delta_f^0 = (\lambda/c_p)/(\rho_u S_u^o)$. As shown in Fig. 6, when the iso-temperature is taken to 600 K for $P_0 = 0.1$ MPa, the theoretical Markstein lengths slightly under-predict the measured data for $\Omega_{C_2H_4} = 0.1$, while for $\Omega_{C_2H_4} = 0.3$, the theoretical Markstein lengths slightly over-predict (under-predict) the measured data for lean (rich) mixtures. With the increase of ambient pressure, the choice of iso-temperature surface in theoretical Markstein length becomes less sensitive while both theoretical and measured Markstein lengths decrease.

Based on them, we reproduced Markstein numbers from Markstein lengths in Fig. 6 and plotted them in Fig. 7. The theoretical (measured) Markstein numbers vary little (appreciably) with ambient pressure. This can be attributed to the flame thickness calculated numerically to obtain the measured Markstein lengths. Several points are worth mentioning here. The theoretical Markstein lengths adopt a global reaction scheme that may not accurately reflect the effects of pressure. Experimentally, the flame displacement speed is defined with respect to the Schlieren boundary. Markstein length can change from negative to positive values when an iso-temperature surface is taken from an unburned temperature to an adiabatic one (see Figs. 5,6 and Figs. S9-S13 in the SM) [54]. An empirical relation of the cold flame front radius (r_u) to the Schlieren boundary radius (r_{sch}, assumed to be the 600 K isotherm) was proposed as $r_u = r_{sch} + 1.95\delta_f^0\sigma^{0.5}$ [36]. However, the application of this empirical relation at elevated pressure is not clear. As shown in Fig. 7, when theoretical and measured Markstein numbers are compared, the flame thickness is needed to obtain experimentally in identifying measured Markstein number. These issues will be explored in future work.

3.4. Onset of cellular instability

Cellular instability in premixed flames is generated by hydrodynamic and/or diffusive-thermal instabilities [37–46], leading to local flame acceleration. This can be roughly evaluated based on the effective Lewis number for diffusive-thermal instability and flame thickness and the thermal expansion ratio for hydrodynamic instability. Sequential images of outwardly propagating spherical premixed flames with CH_4/C_2H_4–air mixtures are shown in Fig. 8 at various $\Omega_{C_2H_4}$ for representative lean ($\phi = 0.8$) and rich ($\phi = 1.2$) cases for $P_u = 0.6$ (a, b) and 0.8 (c, d) MPa. The images were obtained at the moment when the uppermost flame edge reached a specified distance (marked as R_f on the left side) from the center. The heat-release-weighted effective Lewis number, Le_q, the thermal expansion ratio σ, and the flame thickness $\delta_f^0 = (\lambda/c_p)/(\rho_u S_u^o)$ are specified for each image.

The flame surfaces at $P_0 < 0.6$ MPa for $\phi = 0.8$ and 1.2 were smooth during the propagation (although not shown), with the exception of some large cracks due to disturbance from the ignitor. However, fine cells formed over the flame surface at both $\phi = 0.8$ and 1.2 for $P_0 \ge 0.6$ MPa, as shown in Fig. 8. As $\Omega_{C_2H_4}$ increased for $P_0 = 0.6$ and 0.8 MPa, the effective Lewis number increased (but remained close to unity) for both $\phi = 0.8$ and 1.2, such that the contribution of cellular instability due to the imbalance between

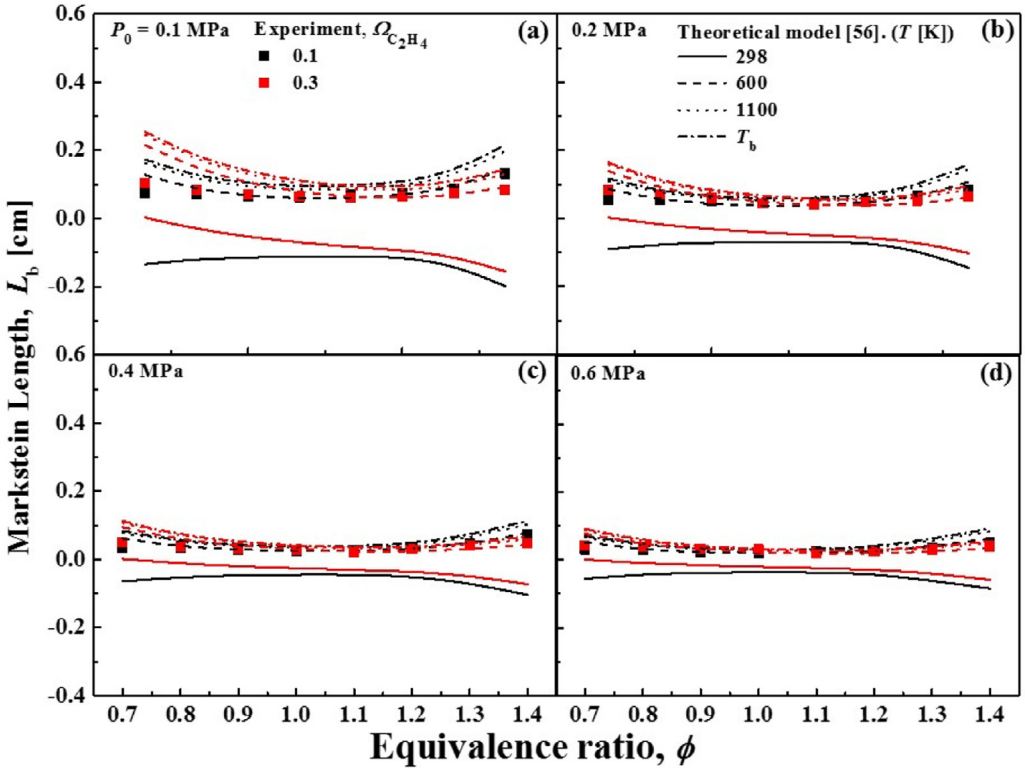

Fig. 5. Measured (symbol) and predicted (lines) Markstein lengths against the equivalence ratio in CH_4/C_2H_4–air premixed flames with $\delta_f^0 = (\lambda/c_p)/(\rho_u S_u^o)$ at elevated pressures. For theoretical Markstein lengths, the temperature-dependent Zel'dovich number and the heat-release-weighted Lewis number are used.

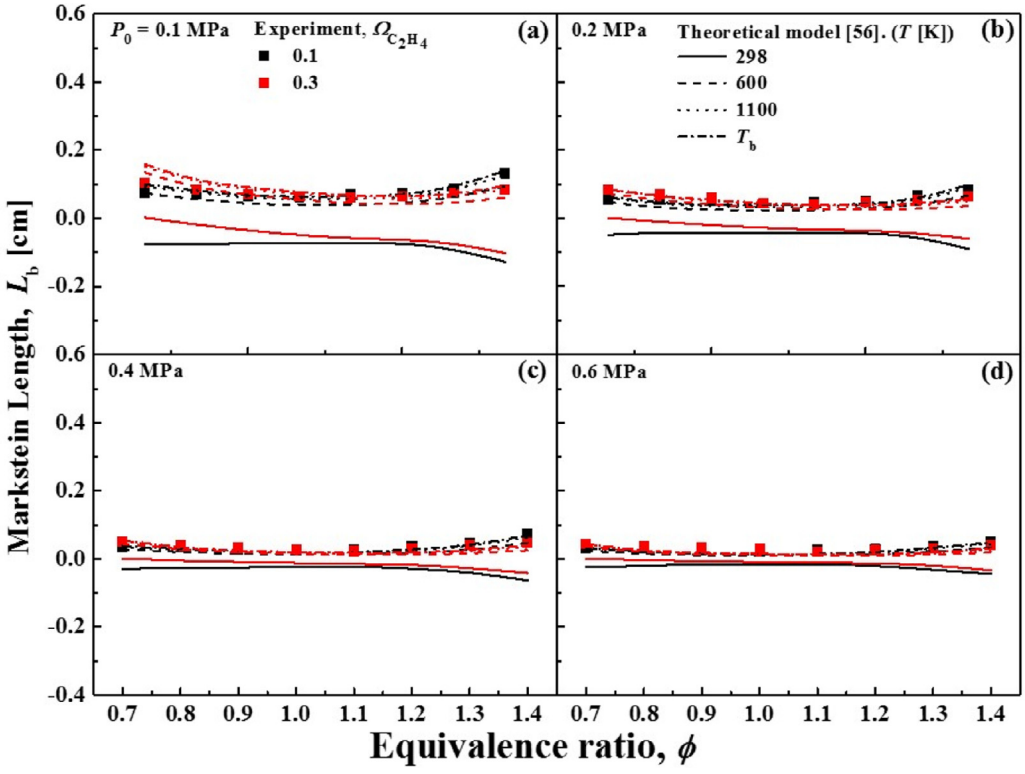

Fig. 6. Measured (symbol) and predicted (lines) Markstein lengths against the equivalence ratio in CH_4/C_2H_4–air premixed flames with $\delta_f^0 = (T_b - T_u)/(\partial T/\partial x)_{max}$ at elevated pressures. For theoretical Markstein lengths, the temperature-dependent Zel'dovich number and the heat-release-weighted Lewis number are used.

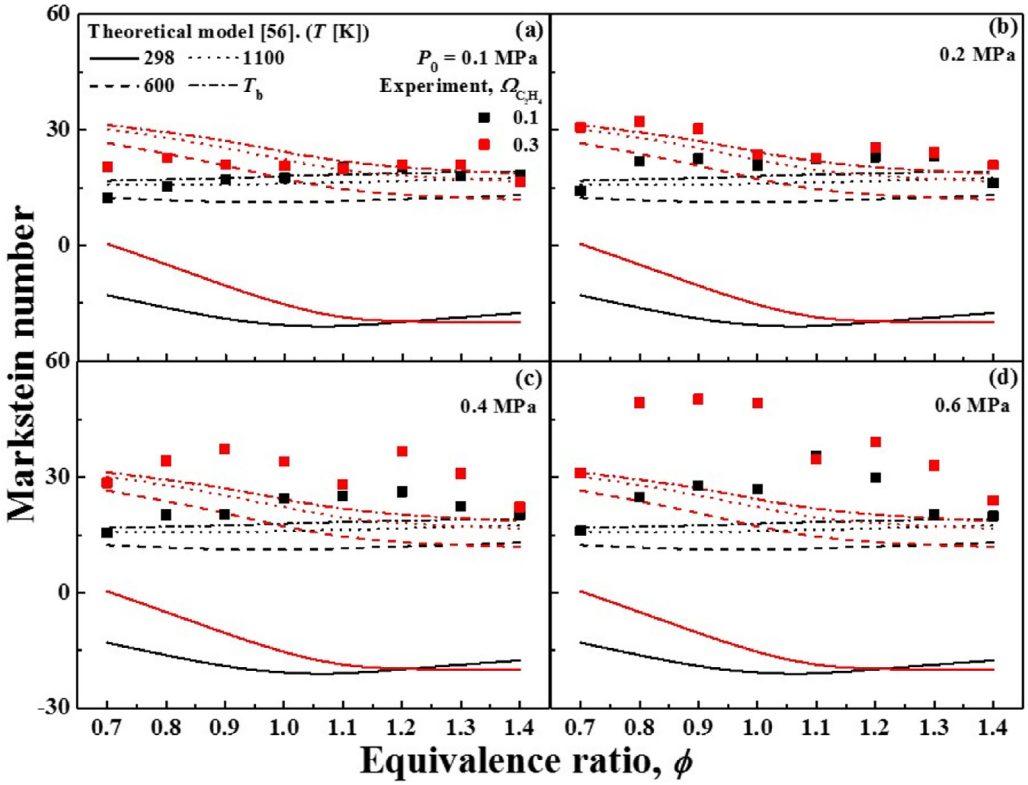

Fig. 7. Measured (symbol) and predicted (lines) Markstein numbers against the equivalence ratio in CH_4/C_2H_4–air premixed flames with $\delta_f^0 = (T_b - T_u)/(\partial T/\partial x)_{max}$ at elevated pressures. For theoretical Markstein lengths, the temperature-dependent Zel'dovich number and the heat-release-weighted Lewis number are used.

mass and thermal diffusivities was mitigated. σ (δ_f^0) increased (decreased) such that hydrodynamic instability was enhanced. Thus the instabilities observed in the present experiment can mainly be attributed to hydrodynamic instability. Increasing the ambient pressure at a fixed $\Omega_{C_2H_4}$ and ϕ, decreases (increases) flame thickness (thermal expansion ratio), thereby enhancing hydrodynamic instabilities.

Further analysis of cellular instability was conducted by investigating the critical flame radius at the onset of cellular instability. The theoretical analysis applied here was developed by Matalon's group [37–39], considering both hydrodynamic and diffusive-thermal instabilities by adopting temperature-dependent transport coefficients. Here, only a brief explanation is provided.

A disturbed flame front can be described by $r = R_f(t)[1 + Z(t)S_k(\theta, \phi)]$, where $Z(t)$ is the amplitude of the disturbance and S_k is the spherical surface harmonics having an integer k. As a flame is expanded, the growth rate (GR) is given by

$$GR = \frac{1}{Z}\frac{dZ}{dt} = \frac{\dot{R}_f}{R_f}\left\{\omega_{DL} - \frac{\delta_f^0}{R_f}[B_1 + \beta(\mathrm{Le}_{eff} - 1)B_2 + \mathrm{Pr}B_3]\right\}. \quad (5)$$

where $\omega_{DL} = (-\sigma + \sqrt{\sigma^3 + \sigma^2 - \sigma})/(\sigma + 1)$ represents the destabilizing effect via thermal expansion, because the thermal expansion ratio (σ) is larger than unity in exothermic reactions. Here, B_1, B_2, and B_3 (refer to the definitions in [37–39]) depend only on σ and k, and they are all positive with the exception of the small values of k. The terms multiplying δ_f^0/R_f denote, respectively, the influences of thermal, molecular, and viscous diffusions [37–39], and Pr represents the Prandtl number. When the effective Lewis number is less than a critical value ($\mathrm{Le}_q^* < 1$), the amplitude grows over time for all wave numbers. In such a case, the instability, which can be developed from a small flame radius, can be judged as diffusive-thermal in nature. Based on these criteria, the cellular instabilities shown in Fig. 8 were not caused by diffusive-thermal ones.

Figure 9 shows the growth rate as a function of wavelength ($\gamma = 2\pi R_f/n$, where n is the wave number) for $\phi = 0.8$ and $P_0 = 0.6$ MPa in case of $\Omega_{C_2H_4} = 0.0$. Here, Pr is not sensitive to temperature, pressure, or $\Omega_{C_2H_4}$; e.g., for $\phi = 0.8$ and $P_0 = 0.8$ MPa, Pr = 0.716 at 298 K and 0.709 at 1200 K in the case of $\Omega_{C_2H_4} = 0.3$ and 0.715 for 298 K in the case of $\Omega_{C_2H_4} = 0$. Thus, Pr was reasonably fixed to 0.71. The flame thicknesses were calculated at 298 K. The results indicate that when R_f is less than 6.9 cm for the CH_4–air premixed flame, the growth rate of the disturbance is always negative, meaning that instability is suppressed. When the flame radius exceeds 6.9 cm, there exists a range of wave lengths where the growth rate becomes positive and the flame becomes unstable due to hydrodynamic effects, e.g., $1.8 < \gamma < 12.5$ mm for $R_f = 15$ cm. The flames with shorter (longer) wavelengths can be stabilized by diffusion (flame stretch) [39].

Further details on the range of cell sizes observed during self-wrinkling can be deduced from Eq. (5), in the form of a marginal stability curve, which is obtained by taking the right-hand side to be zero. Figure 10 presents the results: C-shaped curves were obtained with $\tilde{\lambda} = \text{constant} = 1$ and $\tilde{\lambda} \sim (T/T_u)^{1/2}$ [38] in terms of the wave number n and Peclet number (Pe) defined as $\mathrm{Pe} = R_f/\delta_f^0$. Here, $\tilde{\lambda}$ is the thermal conductivity scaled by its value for the unburned gas side. Thus, Fig. 10 plots results for $\tilde{\lambda} = 1.0$ and 6.0 (corresponding to the thermal expansion ratio for $P_0 = 0.6$ MPa and $\phi = 0.8$, respectively). The region enclosed by each peninsula of Fig. 10 identifies the range of $n_{min} < n < n_{max}$ for a flame radius or Peclet number. Long-wavelength disturbances (large corrugations on the flame surface), corresponding to $n < n_{max}$, are stabilized by flame stretch. Short-wavelength disturbances ($n > n_{max}$) are stabilized by diffusion effects, which tend to smooth out temperature and concentration differences [38,39]. A critical Peclet number, $\mathrm{Pe}_c = R_{cr}\delta_f^0$, can be determined from the turning point

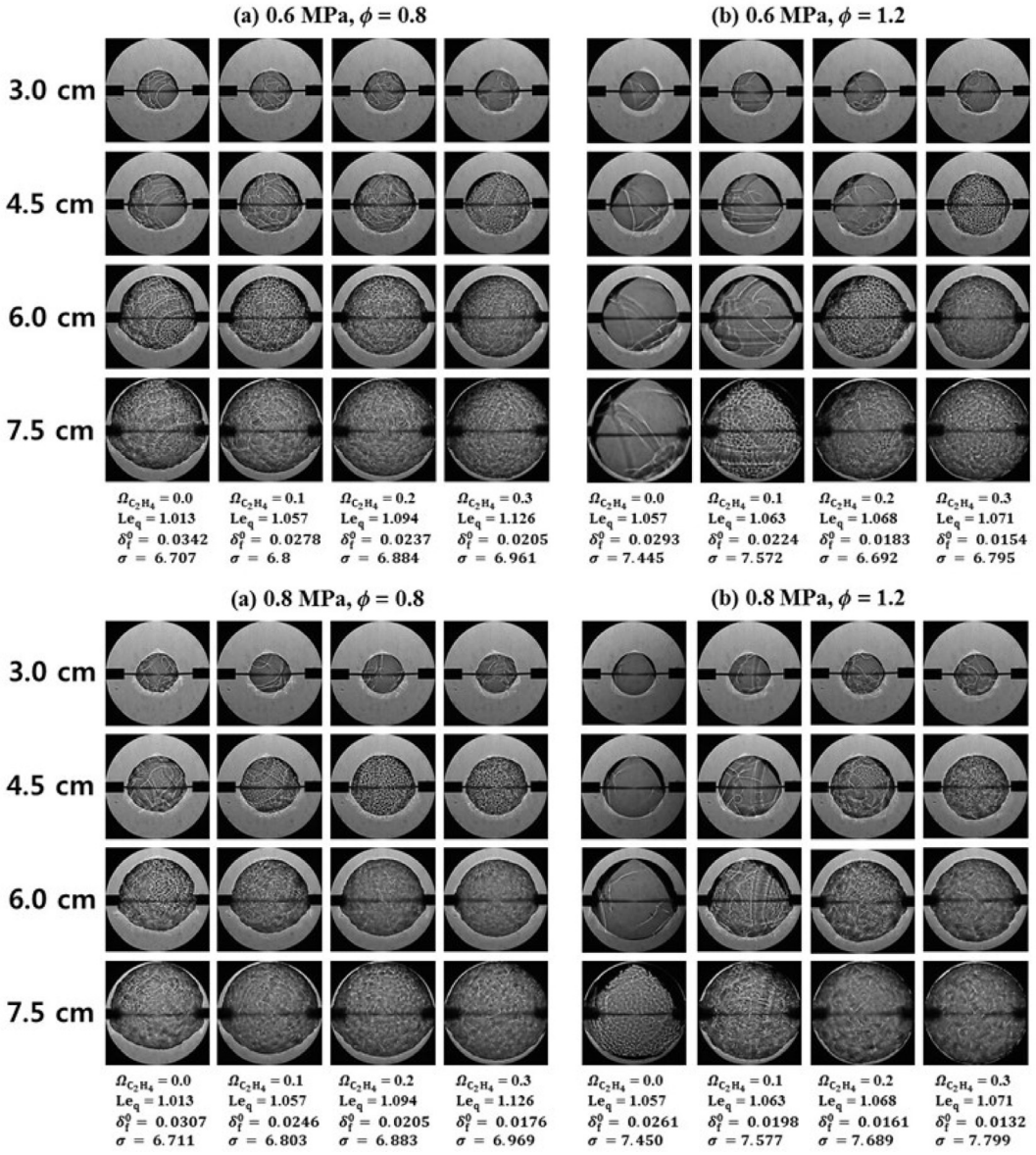

Fig. 8. Effect of ethylene ratio on cellular instability in CH_4/C_2H_4–air premixed flames at ϕ = 0.8 and 1.2 for P_0 = 0.6 (a, b) and 0.8 MPa (c, d).

of the instability peninsular. The upper branch of the peninsula asymptotes to a line, $Pe/n = C$, where the constant C depends on the effective Lewis number [38,39]. The details of determining the constant C have been reported [38]. Thus, the smallest cell size $\gamma_{min} = 2\pi R_f/n \sim 2\pi C\delta_f^0$ scales on the diffusion length, which is dependent on mixture composition. Note that the neutral stability curve can be obtained by setting the right side of Eq. (5) to zero. The lower branch of the peninsula asymptotes to the line n^*_{min} obtained by examining the limit $Pe \to \infty$, namely by setting $\omega_{DL} = 0$. Because the stabilizing mechanism is purely hydrodynamics, the n^*_{min} depends only on σ, and the n^*_{min} asymptotes to 6.6 for all cases in Fig. 10. This value determines the largest theoretical cell size, $\gamma_{max} = 2\pi R_f/n^*_{min}$, which increases linearly with flame radius. Due to the difficulty in experimentally defining cell size, we focused on the critical flame radius for hydrodynamic instability.

As mentioned previously (Fig. 8), the cellular instabilities are not attributed to diffusive-thermal instability but hydrodynamic instability. In such a case, the second terms inside the bracket in Eq. (5) are positive. The growth rate thus depends on burnt flame speed and flame thickness as well as the first term, ω_{DL}. Increasing the ambient pressure at a fixed $\Omega_{C_2H_4}$ and ϕ decreases (increases) flame thickness (thermal expansion ratio), thereby enhancing hydrodynamic instabilities despite reduction of flame speed. Increasing $\Omega_{C_2H_4}$ at a fixed P_0 and ϕ reduces (increases) flame thickness (flame speed) (see Fig. 4 and Figs. S15,16 in the SM).

As shown in Fig. 11, the theoretical critical flame radii determined from Pe_c were compared with measured ones against $\Omega_{C_2H_4}$ at ϕ = 0.8 and 1.2 for P_0 = 0.6 and 0.8 MPa. Here, the experimental critical flame radius is defined as the value at the moment when the burnt laminar propagation speed increases appreciably, and fine cells are simultaneously formed uniformly over a flame surface (see Fig. S9 in the SM) [41]. The error bars were taken as the maximum and minimum values from four experiments. Note that observing cell formation and measuring critical flame radius were limited experimentally within the view of 150-mm-diameter quartz window. The functional relationship of flame radius on chamber pressure [55] can be expressed as

$$(R_f/R)^3 = 1 - \frac{P_{max} - P}{P_{max} - P_0}\left(\frac{P_0}{P}\right)^{\gamma}, \quad (6)$$

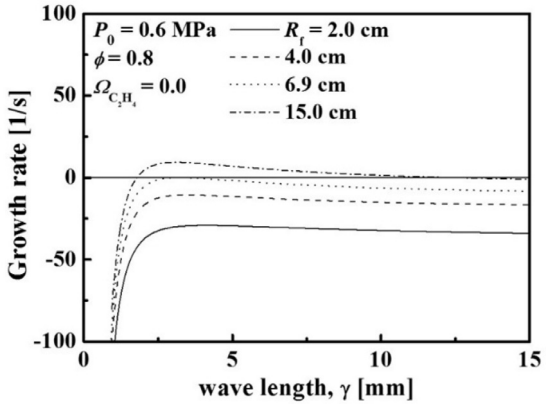

Fig. 9. Growth rate versus wavelength at $\phi = 0.8$ for $P_0 = 0.6$ MPa and $\Omega_{C_2H_4} = 0$.

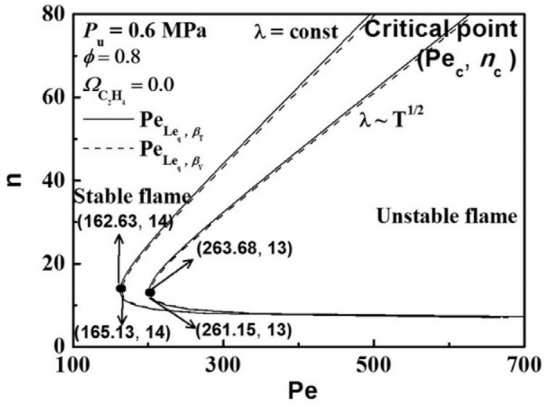

Fig. 10. Peninsular of cellular instability with a functional dependence of wave number upon the Peclet number for $\phi = 0.8$ and $P_0 = 0.6$ MPa in case of $\Omega_{C_2H_4} = 0$.

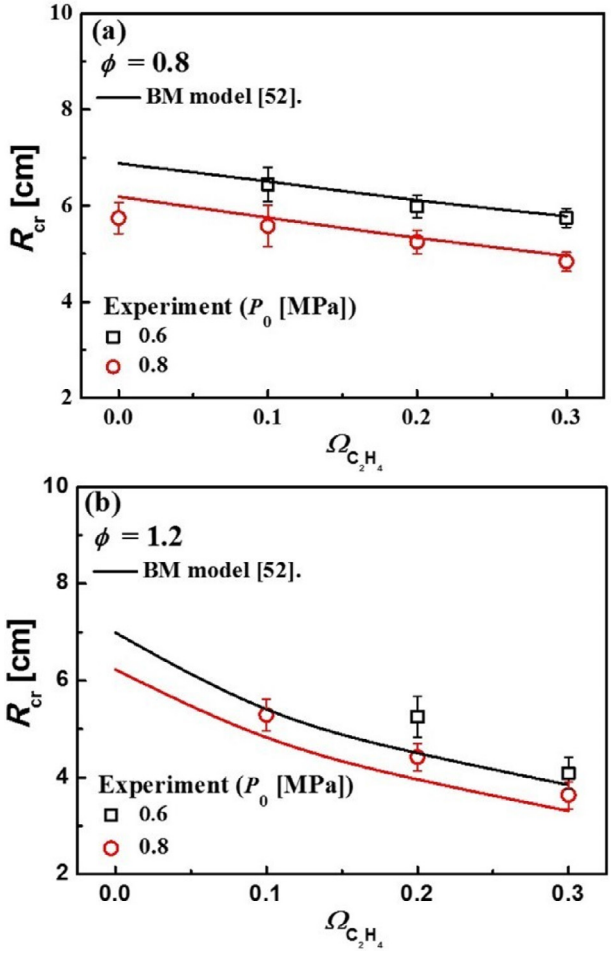

Fig. 11. Measured and theoretical critical radii against $\Omega_{C_2H_4}$ at $\phi = 0.8$ (a) and 1.2 (b) for $P_0 = 0.6$ and 0.8 MPa.

where R, P, and γ denote the chamber radius, the chamber pressure at flame radius R_f, and the specific heat ratio, respectively. With the approximation of $\gamma = 1.4$ (air) and $P_{max} = 8P_0$, the pressure rises at $R_f = 30$ and 70 mm (within the range of observed onset of instability) for $P_0 = 0.8$ MPa are 0.5% and 7.1%, respectively. Thus, the effect of chamber pressure rise is not appreciable in analyzing the onset of cellular instability. Also note that for the range of flame radius monitored, $13.0 \leq R_f \leq 31.0$ mm, the pressure rise effects on laminar flame speed and Markstein length are expected to be minimal. Note that the influence of chamber pressure rise can be larger in measuring the critical flame radius for the onset of cellular instability when the flame radius increases further.

For $P_0 < 0.6$ MPa, the critical flame radius could not be obtained experimentally in the window view. In the case of $\phi = 1.2$, cellular instability was not observed in the window view at $\Omega_{C_2H_4} < 0.2$ for $P_0 = 0.6$ and 0.8 MPa. For $\phi = 0.8$, the critical flame radius could not be obtained for $\Omega_{C_2H_4} < 0.1$ at $P_0 = 0.6$ MPa, but it was observed in all cases for $P_0 = 0.8$ MPa. Both measured and theoretical critical flame radii decreased slightly (rather rapidly) with an increase in $\Omega_{C_2H_4}$ for $\phi = 0.8$ (1.2), implying that increasing $\Omega_{C_2H_4}$ promotes cell formation. The calculated critical flame radii were in reasonably good agreement with the measured ones, while being slightly better than predicted when the temperature-dependent Zel'dovich numbers were used. For $\phi = 1.2$, both predicted critical radii somewhat under-predicted the measured ones, whereas the prediction was close to the measured values for $\phi = 0.8$, with good retracement.

4. Conclusions

An experimental study was conducted to investigate unstretched laminar burning velocity, Markstein length, and cellular instability by varying the ethylene mixing ratio and the chamber pressure up to 0.8 MPa in outwardly propagating spherical CH_4/C_2H_4–air premixed flames. The following conclusions can be made.

(1) The range of flame radius monitored was determined to be $13.0 \leq R_f \leq 31.0$ mm in the present experiment in measuring unstretched laminar burning velocities. The extrapolation model of NM II yielded the best results. Unstretched laminar burning velocities of CH_4/C_2H_4 mixtures were in satisfactory agreement with the numerical results when adopting Aramco Mech 2.0, up to a pressure of 0.6 MPa. Measured laminar flame speeds with respect to the burnt mixture against flame stretch were in reasonable agreement with NM II in both CH_4–air and CH_4/C_2H_4–air premixed flames at normal and elevated pressures.

(2) For the CH_4–air premixed flame, the theoretical Markstein lengths evaluated from the composite model with an iso-temperature of 600 K, $\lambda(x) = x$, and $\delta_f^0 = (T_b - T_u)/(\partial T/\partial x)_{max}$ were in good agreement with the present measured data. The measured Markstein number decreases appreciably (slightly) when the ambient pressure varies from 0.1 to 0.2 (0.2 to 0.6) MPa, while the theoretical Markstein number remains nearly the same

with ambient pressure. For CH_4/C_2H_4–air premixed flame at $P_0 = 0.1$ MPa, the theoretical Markstein lengths slightly under-predict the measured data for $\Omega_{C_2H_4} = 0.1$, while they slightly over-predict (under-predict) the measured data for lean (rich) mixtures for $\Omega_{C_2H_4} = 0.3$. With the increase of ambient pressure, theoretical Markstein length becomes less sensitive to the choice of iso-temperature surface while both theoretical and measured Markstein lengths decrease. The theoretical (measured) Markstein numbers vary little (appreciably) with ambient pressure.

(3) For the CH_4–air premixed flame, cellular instability was not observed at elevated pressures up to 0.6 (0.8) MPa for $\phi = 0.8$ (1.2). For the CH_4/C_2H_4–air premixed flame, cellular instability was enhanced with an increases in the chamber pressure and ethylene/methane mixing ratio, such that the critical flame radius for the onset of cellular instability could be reduced. These findings were mainly attributed to hydrodynamic instability, whereas the effect of diffusive-thermal instability was minor. The theoretical critical flame radii for cellular instability against ethylene mixing ratio were in good agreement with measured values for both lean and rich flame conditions, based on the theoretical model developed by Matalon's group.

Declaration of Competing Interest

(1) Very few data on unstretched laminar burning velocities, Markstein length, and cellular instabilities have been so far reported in CH_4/C_2H_4-air premixed flames. This study covers them in terms of ambient pressure and equivalence ratio, by varying C_2H_4 mixing ratio.

(2) The theoretical Markstein lengths using the composite model from Matalon group were compared with measured data. The capability of predicting the Markstein lengths using the composite model was evaluated by using different definitions of the flame thickness and effective Lewis number, using four iso-surface temperatures, and using three different functional forms of non-dimensional thermal conductivities.

(3) Three different extrapolation models in extracting unstretched laminar burning velocities were tested and the optimized flame radius monitored was investigated. Uncertainty analyses in unstretched laminar burning velocities were made by comparing simulated results using four different reaction mechanisms with measured data.

(4) Measured critical flame radii for cellular instabilities were also compared with those theoretical ones from Matalon's group.

Acknowledgments

This work was conducted under the framework of the Research and Development Program of the Korea Institute of Energy Research (B9-2431). CSY was supported by Basic Science Research Program through the National Research Foundation of Korea (NRF) funded by the Ministry of Science and ICT (NRF-2018R1A2A2A05018901). SHC was supported by the King Abdullah University of Science and Technology (KAUST).

Supplementary material

Supplementary material associated with this article can be found, in the online version, at doi:10.1016/j.combustflame.2020.01.011.

References

[1] Market Report Series: Gas 2018, IEA, 2018, available at http://www.iea.org/topics/naturalgas.
[2] W. Xiao, Y. Huang, Lean blowout limit of a gas turbine combustor operated with aviation fuel and methane, Heat Mass Transf. 52 (5) (2016) 1015–1024.
[3] Y. Lafay, B. Renou, G. Cabot, A. Boukhalfa, Effects of H_2 or CO_2 addition, equivalence ratio, and turbulent straining on turbulent burning velocities for lean premixed methane combustion, Combust. Flame 153 (2008) 510–524.
[4] J.S. Ha, C.W. Moon, J. Park, J.S. Kim, J.H. Yun, S.I. Keel, A study on flame interaction between methane/air and nitrogen-diluted hydrogen–air premixed flames, Int. J. Hydrog. Energy 35 (2010) 6992–7001.
[5] J.S. Kim, J. Park, O.B. Kwon, D.S. Bae, J.H. Yun, S.I. Keel, A study on flame structure and extinction in downstream interaction between lean premixed CH_4-air and (50% H_2 + 50% CO) syngas-air flames, Int. J. Hydrog. Energy 36 (2011) 5717–5728.
[6] F.H.V. Coppens, D.J. Ruyck, A.A. Konnov, The effects of composition on burning velocity and nitric oxide formation in laminar premixed flames of $CH_4 + H_2 + O_2 + N_2$, Combust. Flame 149 (2007) 409–417.
[7] H.S. Guo, G.J. Smallwood, O.L. Gulder, The effect of reformate gas enrichment on extinction limits and No_x formation in counterflow CH_4/air premixed flames, Proc. Combust. Inst. 31 (2007) 1197–1204.
[8] G. Jomaas, X.L. Zheng, D.L. Zhu, C.K. Law, Experimental determination of counterflow ignition temperatures and laminar flame speeds of C_2-C_3 hydrocarbons at atmospheric and elevated pressures, Proc. Combust. Inst. 30 (2005) 193–200.
[9] J.L. Delfau, J. Biet, M. Idir, L. Pillier, C. Vocelle, Experimental and numerical study of premixed, lean ethylene flames, Proc. Combust. Inst. 31 (2007) 357–365.
[10] W. Liu, A.P. Kelly, C.K. Law, Flame propagation and counterflow nonpremixed ignition of mixtures of methane and ethylene, Combust. Flame 157 (2010) 1027–1036.
[11] H.J. Kim, K.H. Van, K.M. Lee, D.G. Lee, Y.T. Kwak, J. Park, Effects of additional diluents on flame propagation speed and Markstein length in outwardly propagating CH_4/C_2H_4 flames, J. Mech. Sci. Technol. 32 (11) (2018) 5537–5544.
[12] Z. Chen, On the accuracy of laminar flame speeds measured from outwardly propagating spherical flames: methane/air at normal temperature and pressure, Combust. Flame 162 (2015) 2442–2453.
[13] S.C. Taylor, Burning velocity and the influence of flame stretch PhD Thesis, University of Leeds, 1991.
[14] F. Halter, T. Tahtouh, C. Mounaïm-Rousselle, Nonlinear effects of stretch on the flame front propagation, Combust. Flame 157 (2010) 1825–1832.
[15] S. Wang, H. Zhang, J. Jarosinski, A. Gorczakowski, J. Podfilipski, Laminar burning velocities and Markstein lengths of premixed methane/air flames near the lean flammability limit in microgravity, Combust. Flame 157 (2010) 667–675.
[16] K.T. Aung, L.K. Tseng, M.A. Ismail, G.M. Faeth, Laminar burning velocities and Markstein numbers of hydrocarbon-air flames, Combust. Flame 102 (1995) 526–530.
[17] M.I. Hassan, K.T. Aung, G.M. Faeth, Measured and predicted properties of laminar premixed methane/air flames at various pressures, Combust. Flame 115 (1998) 539–550.
[18] X.J. Gu, M.Z. Haq, M. Lawes, R. Woolley, Laminar burning velocity and Markstein lengths of methane–air mixtures, Combust. Flame 121 (2000) 41–58.
[19] X. Qin, Y. Ju, Measurements of laminar burning velocities of dimethyl ether and air premixed flames at elevated pressures, Proc. Combust. Inst. 30 (2005) 233–240.
[20] T. Tahtouh, F. Halter, C. Mounaim-Rousselle, Measurement of laminar burning speeds and Markstein lengths using a novel methodology, Combust. Flame 156 (2009) 1735–1743.
[21] W. Lowry, J. de Vries, M. Krejci, E. Petersen, Laminar flame speed measurements and modeling of pure alkanes and alkane blends at elevated pressures, J. Eng. Gas Turb. Power 133 (2011) 091501.
[22] E. Varea, V. Modica, A. Vandel, B. Renou, Measurement of laminar burning velocity and Markstein length relative to fresh gases using a new postprocessing procedure: application to laminar spherical flames for methane, ethanol and isooctane/air mixtures, Combust. Flame 159 (2012) 577–590.
[23] J. Beeckman, L. Cai, H. Pirch, Experimental investigation of the laminar burning velocities of methanol, ethanol, n-propanol, and n-butanol at high pressure, Fuel 117 (214) 340–350.
[24] G.P. Smith, D.M. Golden, M. Frenklach, N.W. Moriarty, B. Eiteneer, M. Goldenberg, C.T. Bowman, R.K. Hanson, S. Song, W.C. Gardiner Jr., V.V. Lissianki, Z. Qin, GRI-MECH 3.0, 1999, available at http://www.me.berkeley.edu/gri_mech.
[25] H. Wang, X. You, A.V. Joshi, S.G. Davis, A. Salkin, F. Egolfopoukos, C.K. Law, USC Mech ii, 2007, <http://ignis.use.edu/USC_II.htm>.
[26] C.J. Sung, B. Li, C.K. Law, H. Wang, Structure and sooting limits in counterflow methane/air and propane/air diffusion flames from 1 to 5 atmospheres, Proc. Combust. Inst. 27 (1998) 1523–1530.
[27] C.-W. Zhou, Y. Li, E. O'Connor, K.P. Somers, S. Thion, C. Keesee, O. Mathieu, E.L. Petersen, T.A. DeVerter, M.A. Oehlschlaeger, G. Kukkadapu, C.-J. Sung, M. Alrefae, F. Khaled, A. Farooq, P. Dirrenberger, P.-A. Glaude, F. Battin-Leclerc, J. Santner, Y. Ju, T. Held, F.M. Haas, F.L. Dryer, H.J. Curran, A comprehensive experimental and modeling study of isobutene oxidation, Combust. Flame 167 (2016) 353–379.
[28] D. Bradley, R.A. Hicks, M. Lawes, C.G.W. Sheppard, R. Wooley, The measurement of laminar burning velocities and Markstein numbers for iso-octane–air

and iso-octane–n-heptane–air mixtures at elevated temperatures and pressures in an explosion bomb, Combust. Flame 115 (1998) 126–144.
[29] G. Rozenchan, D.L. Zhu, C.K. Law, S.D. Tse, Outward propagation, burning velocities, and chemical effects of methane flames up to 60 atm, Proc. Combust. Inst. 29 (2003) 1461–1470.
[30] F. Halter, C. Chauveau, N. Djebaili-Chaumeix, I. Gokalp, Characterization of the effects of pressure and hydrogen concentration on laminar burning velocities of methane–hydrogen–air mixtures, Proc. Combust. Inst. 30 (2005) 201–208.
[31] G.H. Markstein, Experimental and theoretical studies of flame-front stability, Aeronaut. Sci. 18 (1951) 199–209.
[32] M.L. Frankel, G.I. Sivashinsky, On effects due to thermal expansion and Lewis number in spherical flame propagation, Combust. Sci. Tech 31 (1983) 131–138.
[33] P.D. Ronney, G.I. Sivashinsky, A theoretical study of propagation and extinction of nonsteady spherical flame fronts, SIAM J. Appl. Math. 49 (1989) 1029–1046.
[34] J.K. Bechtold, C. Cui, M. Matalon, The role of radiative losses in self-extinguishing and self-wrinkling flames, Proc. Combust. Inst. 30 (2005) 177–184.
[35] A.P. Kelley, C.K. Law, Nonlinear effects in the extraction of laminar flame speeds from expanding spherical flames, Combust. Flame 156 (2009) 1844–1851.
[36] D. Bradley, P. Gaskell, X. Gu, Burning velocities, Markstein lengths, and flame quenching for spherical methane-air flames: a computational study, Combust. Flame 104 (1) (1996) 176–198.
[37] M. Matalon, B.J. Matkowsky, Flames as gas dynamic discontinuities, J. Fluid Mech. 124 (1982) 239–259.
[38] R. Addabbo, J.K. Bechtold, M. Matalon, Wrinkling of spherically expanding flames, Proc. Combust. Inst. 29 (2002) 1527–1535.
[39] M. Matalon, Intrinsic flame instabilities in premixed and nonpremixed combustion, Ann. Rev. Fluid Mech. 39 (2007) 163–191.
[40] S. Kadowaki, H. Suzuki, H. Kobayashi, The unstable behavior of cellular premixed flames induced by intrinsic instability, Proc. Combust. Inst. 30 (2005) 169–176.
[41] O.C. Kwon, G. Rozenchan, C.K. Law, Cellular instabilities and self-acceleration of outwardly propagating spherical flames, Proc. Combust. Inst. 29 (2002) 1775–1783.
[42] G.I. Sivashinsky, Diffusional-thermal theory of cellular flames, Combust. Sci. Tech. 15 (1977) 137–146.
[43] C.K. Law, G. Jomaas, J.K. Bechtold, Diffusional-thermal theory of cellular flames, Proc. Combust. Inst. 30 (2005) 159–167.
[44] T.M. Vu, W.S. Song, J. Park, Measurements of propagation speeds and flame instabilities in biomass derived gas-air premixed flames, Int. J. Hydrogen Energy 36 (2011) 12058–12067.
[45] T.M. Vu, J. Park, J.S. Kim, O.B. Kwon, Experimental study on cellular instabilities in hydrocarbon/hydrogen/carbon monoxide-air premixed flames, Int. J. Hydrog. Energy 36 (2011) 6914–6924.
[46] T.M. Vu, J. Park, O.B. Kwon, J.H. Yun, S.I. Keel, Effects of diluents on cellular instabilities in outwardly propagating spherical syngas–air premixed flames, Int. J. Hydrog. Energy 35 (2010) 3868–3880.
[47] E. Hu, Z. Huang, J. He, J. Zheng, H. Miao, Measurements of laminar burning velocities and onset of cellular instabilities of methane-hydrogen-air flames at elevated pressures and temperatures, Int. J. Hydrog. Energy 34 (2009) 5574–5584.
[48] Y. Xie, J. Wang, X. Cai, Z. Huang, Self-acceleration of cellular flames and laminar flame speed of syngas/air mixtures at elevated pressures, Int. J. Hydrog. Energy 41 (2016) 18250–18258.
[49] Z. Chen, C. Tang, J. Fu, X. Jiang, L. Wei, Z. Huang, Experimental and numerical investigation on diluted DME flames: thermal and chemical kinetic effects on laminar flame speeds, Fuel 102 (2012) 567–573.
[50] Q. Zhou, C.S. Cheng, C.W. Leung, X. Li, Z. Huang, Effects of diluents on laminar burning characteristics of bio-syngas at elevated pressures, Fuel 248 (2019) 8–15.
[51] Z. Chen, Y. Ju, Theoretical analysis of the evolution from ignition kernel to flame ball and planar flame, Combust. Theory Model. 11 (2007) 427–453.
[52] Z. Chen, On the extraction of laminar flame speed and Markstein length from outwardly propagating spherical flames, Combust. Flame 158 (2011) 291–300.
[53] J.K. Bechtold, M. Matalon, The dependence of the markstein length on stoichiometry, Combust. Flame 127 (2001) 1906–1913.
[54] G.K. Giannakopoulos, A. Gazoulis, C. Frouzakis, M. Matalon, A.G. Tomboulides, Consistent definitions of “flame displacement speed” and “Markstein length” for premixed flame propagation, Combust. Flame 162 (2015) 1249–1264.
[55] A.E. Dahoe, Laminar burning velocities of hydrogen-air mixtures from closed vessel gas explosions, J. Loss Prev. Process Ind. 18 (2005) 152–166.